

Plume Origins and Plumbing: From Ocean to Surface

J. R. Spencer

Southwest Research Institute

F. Nimmo

University of California, Santa Cruz

A. P. Ingersoll

California Institute of Technology

T. A. Hurford

NASA Goddard Space Flight Center

E. S. Kite

University of Chicago

A. R. Rhoden

Southwest Research Institute

J. Schmidt

University of Oulu

C. J. A. Howett

Southwest Research Institute

The plume of Enceladus provides a unique window into subsurface processes in the ice shell and ocean of an icy world. Thanks to a decade of observations and modeling, a coherent picture is emerging of a thin ice shell extending across the south polar region, cut through by fractures directly connected to the underlying ocean, and at least partially filled with water. The plume jets emerging from the fractures directly sample this water reservoir. The shell undergoes daily tidal flexing, which modulates plume activity by opening and closing the fractures. Dissipation in the ice and conduit water components due to this flexing is likely to generate the several gigawatts of observed power that are lost from the south pole as infrared radiation and plume latent heat.

1. INTRODUCTION

Since the discovery of activity at the south pole of Enceladus, enormous progress has been made in interpreting the rich data from the multiple instruments on the Cassini spacecraft to understand what is happening below the visible surface. In this chapter, we review the visible and thermal observations of the surface expression of the plume fractures. We then review the current state of understanding of the processes that connect the surface to the underlying ocean, constrained by these observations and by the properties of the plume itself, which are described in more detail in the chapter in this volume by Goldstein et al.

2. SURFACE OBSERVATIONAL CONSTRAINTS

2.1. Plume Source and Jet Morphology

The plume emanates from four prominent parallel fractures, informally named the “tiger stripes,” and associated branches. These fractures are approximately 130 km long and spaced 35 km apart, aligned approximately 30° westward from the direction to Saturn. The major tiger stripe fractures have raised margins enclosing a central trough approximately 2 km wide and 0.5 km deep, although some plume jets and thermal emission emanate from simple open fractures without raised margins or complex structure. These

troughs are the source of both the thermal emission (Spencer *et al.*, 2006; Spencer and Nimmo, 2013) and the plume jets (Spitale and Porco, 2007; Porco *et al.*, 2014; Spitale *et al.*, 2015; Helfenstein and Porco, 2015). The fractures themselves are unresolved at the ~ 10 -m/pixel resolution of the best Cassini ISS images, appearing only as dark linear features at the bottom of narrow trenches within the tiger stripes. In some locations there are multiple trenches, separated by medial ridges, within the tiger stripe trough (Helfenstein and Porco, 2015) (see also Fig. 1f). The ice-particle plume consists of a combination of continuous curtains (Spitale *et al.*, 2015) and at least 100 discrete jets (Porco *et al.*, 2014). The source locations on the surface of the discrete jets are not in general obvious in the available ISS images of the tiger stripes, although some appear to be associated with radial grooves or cross-cutting fractures (Helfenstein and Porco, 2015). Individual jets are time-variable in ways that are not obviously related to the tidal modulation of the plume as a whole (Porco *et al.*, 2014). Discrete jets of water vapor are also seen in the UV stellar occultation data (Hansen *et al.*, 2011, 2017).

2.2. Spatial Distribution of Thermal Emission

At 10 km resolution thermal emission is present along the entire length of the tiger stripes where plume activity is seen (Howett *et al.*, 2011) (see also Fig. 1). One striking example is a branch of Baghdad Sulcus that is much narrower and less conspicuous in ISS images than some of its inactive neighbors, but is a site of both thermal emission and plume activity (points 75–80 in Fig. 3). However, emission strength varies greatly along the fractures, being particularly strong toward the Saturn-facing ends of Damascus and Baghdad Sulci and to a lesser extent at the anti-Saturn end of Alexandria Sulcus, where some fractures perpendicular to the main tiger stripes are also active. At higher spatial resolution, larger local spatial variations in emission strength are seen. Figure 1 shows the appearance of the tiger stripes at visible and thermal wavelengths at a variety of scales. On 1-km scales, thermal emission shows peaks that, in the few places where data of sufficient quality exist, correspond in some locations (but not all) to discrete plume jets seen by ISS (Fig. 1b, Fig. 2a). Similar discrete peaks of thermal emission, corresponding to plume jet locations, are seen by Cassini's VIMS instrument at $5\ \mu\text{m}$ (Goguen *et al.*, 2013, 2016). Excess 2.2-cm thermal emission has also been reported via passive radiometry and radar-derived emissivities from the Cassini RADAR instrument near 60°S , 240°W and 65°S , 340°W , just north of the tiger stripe region (Le Gall *et al.*, 2017).

2.3. Tiger Stripe Temperatures

Peak temperatures along the tiger stripes have been measured both by CIRS and VIMS by fitting blackbody curves to tiger stripe emission spectra, with similar results. The width of the emitting region can also be derived by assuming a linear source parallel to the fractures, which varies greatly

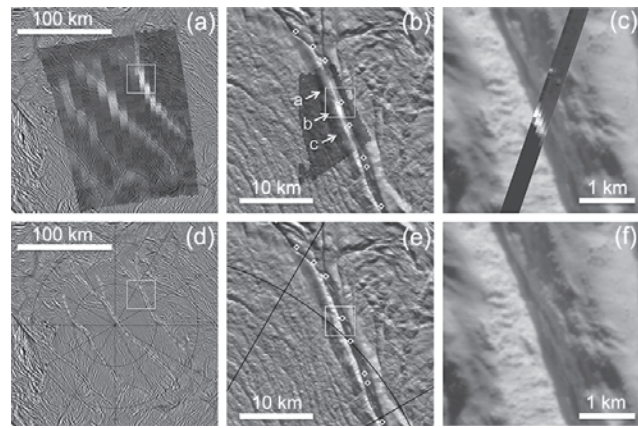


Fig. 1. See Plate 19 for color version. The appearance of the tiger stripes in the visible (Cassini ISS) and thermal infrared [Cassini CIRS, 7–16 μm , (a)–(c)] at a variety of scales. (a) The entire tiger stripe system with the exception of part of Alexandria Sulcus (left), which is known from other observations to be relatively faint. CIRS 9–16- μm data from March 2008. Dashed lines mark the location of the active tiger stripes. The square shows the location of (b). (b) Closeup of the most active part of Damascus Sulcus (a combination of 9–16- μm and 7–9- μm images), mapped by CIRS in August 2010. Diamonds show the location of ISS plume jets reported by Helfenstein and Porco (2015). Arrows mark the locations of three discrete hot spots, a, b, and c (also shown in Fig. 2a), two of which correspond well to plume jet locations. The square shows the location of (c). (c) The highest-resolution CIRS image of Damascus Sulcus emission, taken by direct sampling of the CIRS 7–9- μm interferograms from October 2015, showing dominant emission from a single fissure <100 m wide, and isolated hot spots elsewhere within the central trough (Gorius *et al.*, 2015). Placement relative to the terrain is approximate. (d)–(f) The same images without the CIRS data overlay, to show the terrain more clearly.

from place to place. Goguen *et al.* (2013) obtained a best-fit isothermal temperature of 197 ± 20 K, with a best-fit width of 9 m, from 4–5- μm spectra of one location on Baghdad Sulcus (Fig. 2c), and Spencer *et al.* (2011) obtained a temperature of 176.7 ± 1.3 K, with a best-fit width of 147 m, from 7–9- μm spectra of the brightest point on Damascus Sulcus (Fig. 2b). The fact that longer wavelengths tend to produce fits with lower temperatures (e.g., the best fit of 167 ± 0.7 K to the full 600–1400- cm^{-1} wavelength range in Fig. 2b) suggests that the surface near the tiger stripes has (not surprisingly) a range of temperatures. The fact that temperatures higher than 200 K have not been seen, despite evidence for liquid water at depth, is plausibly due to rapid sublimation and evaporative cooling of the water ice surface at the vents (Goguen *et al.*, 2013), which would tend to buffer water ice surface temperatures due to the strong dependence of sublimation rate on temperature. In theory, lag deposits or other impermeable coatings of non-volatile materials, such as salts, could suppress sublimation cooling and allow higher temperatures; the lack of observed higher temperatures may indicate that such coatings are uncommon.

The spatial distribution of emission as a function of distance from the vents has been compared to simple models of conduction away from a warm, isothermal, vertical fracture by *Abramov and Spencer (2009)*. The intensity and wavelength distribution of the thermal emission spectrum of the warmest part of Damascus, taken in August 2010, can be

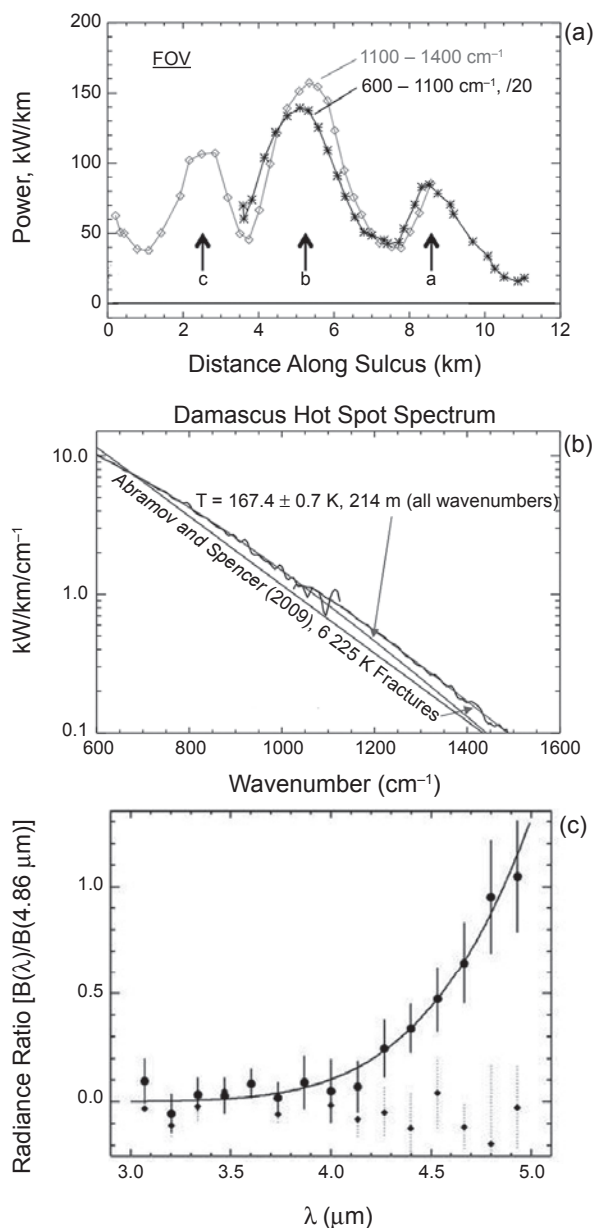


Fig. 2. (a) Power profile along Damascus sulcus in two CIRS wavebands, showing peaks associated (in two cases) with ISS jets, from the data shown in Fig. 1b. Arrows identify the same three discrete hot spots, a, b, and c. (b) CIRS spectrum of the brightest part of Damascus Sulcus [peak near 5 km (*Spencer et al., 2011*)], compared to blackbody fits and the model of *Abramov and Spencer (2009)*, multiplied sixfold to approximate the signature of six adjacent fractures. (c) VIMS spectrum of Baghdad Sulcus, compared to blackbody fit with temperature 197 K (*Goguen et al., 2013*). The diamonds show the mean of background measurements obtained on either side of the Sulcus.

matched quite well with such models, assuming a fracture temperature of 225 K, except that up to six parallel fractures within the ~1-km width of the CIRS footprint are required (Fig. 2b). Forty-meter resolution imaging of a nearby region in October 2015 (Fig. 1c) shows extended thermal emission consistent with the presence of multiple active fractures, but emission is dominated by a single fracture. This region may not correspond precisely to the region of the spectrum in Fig. 2b, or emission may be time-variable.

The thermal observations discussed above are at wavelengths shorter than 16.7 μm (600 cm⁻¹), where both CIRS and VIMS have relatively high spatial resolution. However, most of the thermal emission from the fractures is radiated at longer wavelengths. Understanding this long-wavelength emission is important to determine both the lower-temperature emission from the stripes and their total heat flow. Unfortunately, the long-wavelength (10–600 cm⁻¹) detector of the CIRS instrument has much lower spatial resolution than the short-wavelength detectors, and can resolve the tiger stripes only for brief intervals during the closest Cassini flybys. Models are thus required to extrapolate these limited long-wavelength resolved observations to the entire tiger stripe system. *Spencer et al. (2013)* found that the available high-resolution 10–600-cm⁻¹ observations could be matched by adding a low-temperature emission component, with a temperature of 80 K, to the higher-temperature emission inferred at shorter wavelengths. Adjusting the local width of this low-temperature component to match the observations, and extrapolating to the rest of the tiger stripe system by assuming a constant 80 K temperature, and assuming that the spatial variation in the radiated power for the long-wavelength emission was similar to that of the well-mapped short-wavelength emission (Fig. 1a), *Spencer et al. (2013)* derived a complete model of observed emission from the tiger stripes, updated slightly here, that is consistent with, although certainly not uniquely constrained by, the available data (Fig. 3).

2.4. Total Heat Flow

Total heat flow from the tiger stripe system, an important geophysical parameter, has been difficult to determine precisely. Blackbody fits to the first 600–1100 cm⁻¹ integrated CIRS spectra of the entire tiger stripe system in 2005 produced a heat flow of 5.8 ± 1.9 GW (*Spencer et al., 2006*). Subsequent integrated 10–600-cm⁻¹ observations of the south polar terrain (SPT) indicated much higher heat flow (15.8 ± 3.1 GW), but required model-dependent subtraction of the “passive” contribution from re-radiated sunlight (*Howett et al., 2011*). Because it is highly likely that the emission associated with the tiger stripes fractures themselves is endogenic, fracture emission provides a lower limit to the total endogenic component (this is a lower limit because there may also be endogenic emission from between the tiger stripes, either from smaller unresolved fractures or from conduction through the ice shell that raises the background temperature). The model of *Spencer et al. (2013)*, described above (Fig. 3), produces a tiger stripe radiated heat flow of 4.2 GW. Note that

this number includes a passive component due to solar heating of the radiating regions [the so-called “thermal pedestal effect” (Veeder *et al.* 1994)], which when subtracted might

reduce the total by a few tenths of a gigawatt. To this must be added the latent heat content of the water vapor plume [~ 0.5 GW (Ingersoll and Pankine, 2010)], and any additional

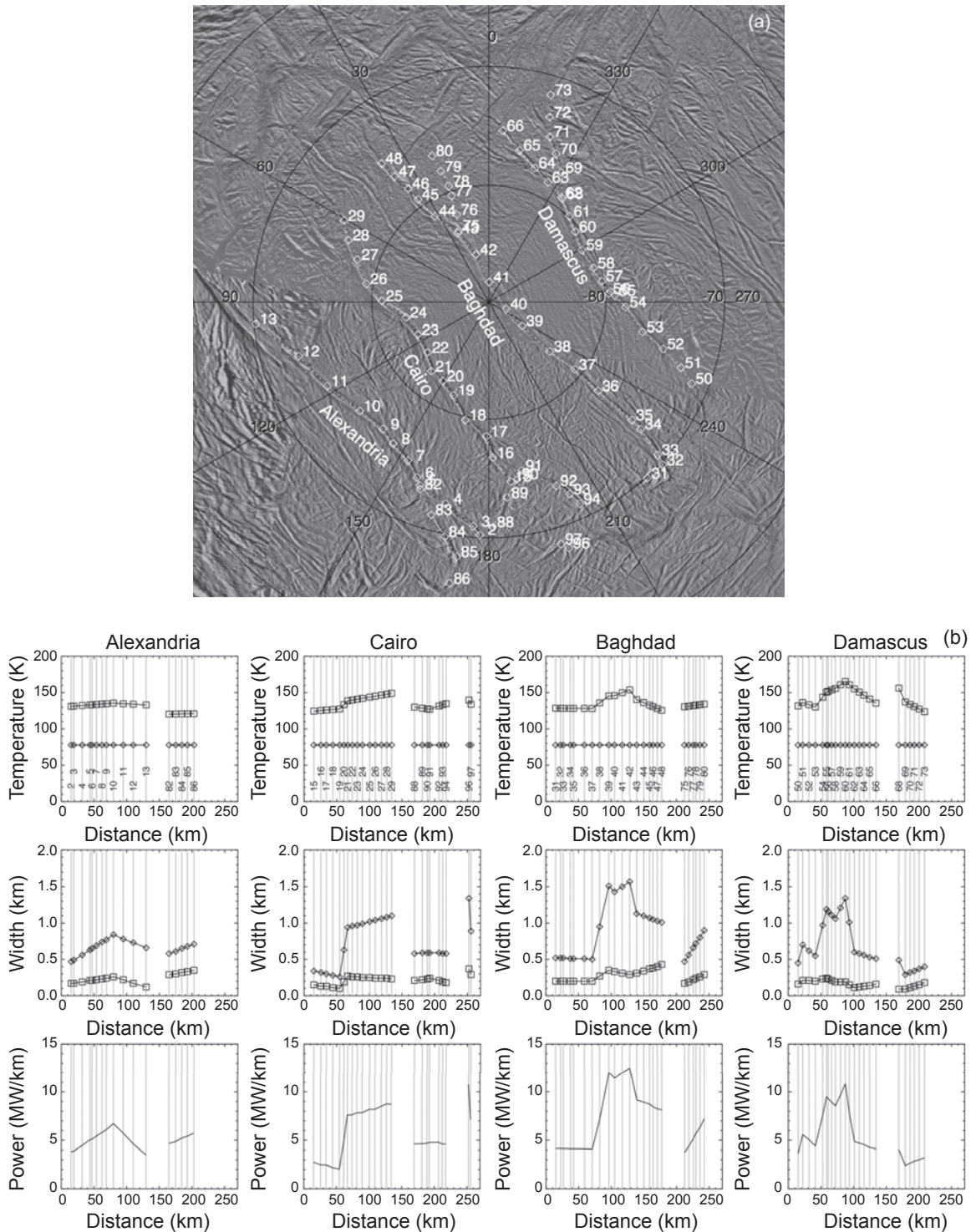


Fig. 3. Model of thermal emission from the tiger stripes, matched to multiple CIRS datasets, updated from *Spencer et al.* (2013). **(a)** Locations of the warm material along the fractures. Numbered points correspond locations in the model where the model parameters are defined, and correspond to numbered vertical lines in **(b)**. **(b)** Model temperatures, emission widths, and power per unit stripe length at each of those points along the four named tiger stripes and their branches. Inflection points in the model parameters are locations where the model parameters were fit to the multiple datasets; intermediate points are linearly interpolated. This model produces a total radiated heat flow of 4.2 GW.

broadly distributed endogenic radiation from the surface between and surrounding the tiger stripes. The discrepancy between the >13-GW estimates for the total heat flow and the ~4.2-GW tiger stripe heat flow suggests the existence of this broad component, but it is difficult to measure. For instance, the heat conducted up from the ocean through 2 km of ice with thermal conductivity $3.5 \text{ W m}^{-1} \text{ K}^{-1}$ would raise the temperature of the surface from 73 K to 77 K, which would be difficult to detect without a well-constrained model of passive thermal emission. If this heat flux were constant from the pole to 75°S latitude, the total endogenic power would be an additional ~4.7 GW.

3. THE NATURE OF THE PLUME SOURCE

Figure 4 summarizes our current picture of the subsurface configuration of the tiger stripe fractures, and the principle processes operating there. These are discussed in more detail below.

3.1. Is the Plume Source Solid or Liquid?

The detection of plumes emanating from fractures in the SPT of Enceladus (Dougherty et al., 2006; Porco et al., 2006; Spencer et al., 2006; Spitale and Porco, 2007) led to multiple physical models of the eruptions. The earliest models invoked either a rapidly boiling, near-surface liquid water reservoir (Porco et al., 2006), degassing of clathrates (Kieffer et al., 2006), or direct sublimation from warm ice (Nimmo et al., 2007). Over time, measurements of the composition, structure, and density of the plumes have favored a liquid water source, as described in detail below.

Enceladus' plumes are composed of solid particles that are mainly water ice, along with a gaseous component that is dominated by water vapor (see the chapter in this volume by Goldstein et al.). Minor components of the plume gases include CO_2 , NH_3 , CH_4 , H_2 , heavier hydrocarbons, and other species (Waite et al., 2009; Hansen et al., 2011; Waite et al., 2017). These minor gas species are suggestive of hydrothermal cycling between the rocky interior and cryosphere (e.g., Matson et al., 2007; Glein et al., 2008; see the chapters in this volume by Glein et al. and Postberg et al.).

The presence of sodium and potassium salts in the plume and E-ring particles (Postberg et al., 2009), especially in larger, lower-speed particles found preferentially near the plume source (Postberg et al., 2011), is strong evidence of a liquid source. If the particles were formed by condensation from the vapor, which had sublimated from ice, they would be practically salt-free. Hence, salt-bearing plume particles would not be expected in “dry” models (e.g., Kieffer et al., 2006; Loeffler et al., 2006; Nimmo et al., 2007; Cooper et al., 2009). Liquid water interacting with silicates will result in dissolved salts; as the water freezes slowly, the salts become progressively more concentrated in the liquid, while the ice remains salt-free. Frozen droplets derived from the liquid will retain the salt content. The salty grains imply direct connections between the liquid ocean and the vacuum of space.

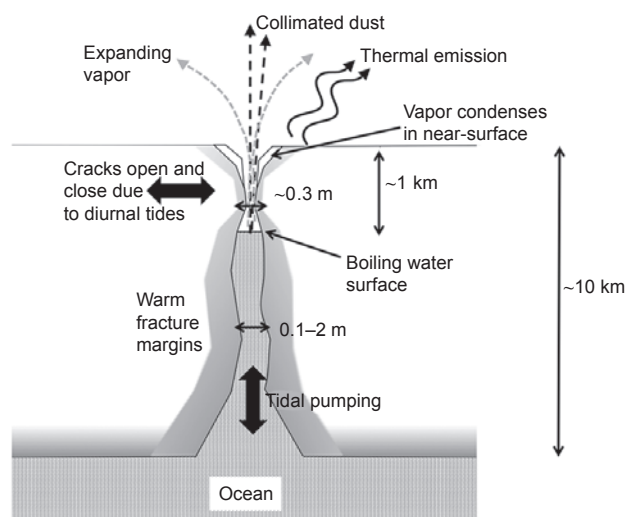


Fig. 4. Schematic of the major processes, discussed in detail in this chapter, thought to be taking place in the plumbing connecting the surface tiger stripes to the underlying ocean.

Cassini’s Cosmic Dust Analyzer (CDA) also identified nanometer-sized grains rich in silicon (Hsu et al., 2015) that are most likely SiO_2 . Their size and composition suggest formation in a hydrothermal system within Enceladus, further supporting a liquid water source for the plumes that is in contact with rock (Glein et al., 2008; Hsu et al., 2015). Hydrothermal SiO_2 particles will grow to micrometer-sized, larger than is observed, over thousands of years, which may be evidence that the production of nanosilica grains is very recent or even ongoing. The nanosilica particles further constrain the deep ocean conditions to moderate salinity, an alkaline pH, and relatively warm temperature (Hsu et al., 2015; Sekine et al., 2015). However, the exact values depend on many assumptions, including the composition of Enceladus’ rocky core and whether the system is chemically open or closed (Sekine et al., 2015; Glein et al., 2015).

The total particulate mass within the plumes and the ratio of ice to vapor both provide clues as to the source of the plume material. Early attempts to constrain the relative abundances of ice to vapor resulted in quite disparate values, with Porco et al. (2006) reporting a high abundance that favored a liquid source and Kieffer et al. (2009) finding a low value that suggested a sublimation-driven process of plume formation. Estimates using high-phase-angle Cassini images suggested a large solid/gas ratio of 0.35–0.7 if particles are spherical (Ingersoll and Ewald, 2011), more consistent with an evaporating liquid source, but much lower ratios, 0.07 ± 0.01 , if most particles are aggregates (Gao et al., 2016). As discussed below, this picture may be complicated by the presence of different eruptive sources, with different solid/gas ratios. For instance, there may be a “background” component of vapor flux with very little solid material (Postberg et al., 2009, 2011). Nonetheless, the compositional measurements suggest that, overall, the liquid source is dominant.

3.2. Plume Plumbing and Source

3.2.1. The plumbing system problem. The plumes, and thus their plumbing system, appear to be long-lived phenomena (see the chapter by Goldstein et al. in this volume). In order to reach the surface as a plume of ice grains and vapor, Enceladus ocean water faces an uphill struggle. First, ocean-to-surface conduits must penetrate the ice shell; second, the conduits must be kept open in spite of ice creep; third, water must flow through the shell without freezing; and fourth, water must overcome its greater density relative to the surrounding ice. These challenges define the plumbing-system problem for eruptions on Enceladus.

Ocean-to-surface conduits thread through the cold near-surface layer of the ice shell, where ice creep is negligible but conduits may seal off by freezing shut. Conduits also pass through the warmer near-ocean layer, where conduits are vulnerable to closure by ice creep. Near the surface, magmatic eruptions are the best terrestrial analogs (e.g., Rubin 1995). Near the ocean, englacial channels are the best terrestrial analogs (Cuffey and Patterson, 2010). Ice shell thickness (D) at the SPT is <45 km but is more likely <10 km (Jess et al., 2014; Čadež et al., 2016; Hemingway et al., this volume). By simple buoyancy arguments, the time-averaged water table depth for a non-overpressured, volatile-free ocean is a distance $0.1 D$ below the surface. Ocean overpressure, diurnal tides, or siphoning by bubble exsolution, could all spill water onto the surface, although there is no evidence from geomorphology or IR data, where observed temperatures peak at ~ 200 K as discussed above, for liquid water reaching the surface today.

Forming an ocean-to-surface conduit from a crack that initiates at the surface would require tensile stresses that exceed overburden pressure (Crawford and Stevenson, 1988). Therefore, if the only source of stress is diurnal eccentricity-tide stresses of $\sim 10^5$ Pa (Nimmo et al., 2007), surface-initiated cracks on Enceladus have zero width below a depth of 1 km. Stresses $\gg 10^5$ Pa are possible with non-synchronous rotation, polar wander or ice shell freezing, but these stresses develop over long timescales and so will relax away in the ductile, lower part of the shell (Crawford and Stevenson, 1988). Despite this relaxation effect, fractures that initiate at the surface can propagate under these larger stresses to the ocean for $D < 25$ km and ice tensile strength 3 MPa (Rudolph and Manga, 2009). Water-filled cracks that initiate at the ocean can puncture the shell more readily than cracks that initiate at the surface, and ice can fracture even close to its melting point (Schulson, 2001). That is because the crack-closing stress is the pressure-head difference between the ice column and the water column, which is more favorable than the pressure-head difference between ice and vacuum (Crawford and Stevenson, 1988; Matson et al., 2012). Gas exsolution can contribute to the buoyancy of the rising water column (Crawford and Stevenson, 1988). Furthermore, the ocean may be overpressured (Manga and Wang, 2007), favoring crack propagation. If $D \lesssim 10$ km, conduits could form at the current orbital eccentricity. Alternatively, con-

duits may have formed during a higher-eccentricity period in Enceladus' past, when stresses were higher.

A pre-existing ocean to surface conduit can be sealed by ice creep, driven by the pressure difference, ΔP , between the water column and the surrounding lithostatic pressure. For a cylindrical pipe of radius R , the pipe-closing rate is (Nye, 1953; Cuffey and Patterson, 2010)

$$\frac{1}{R} \frac{\partial R}{\partial t} = A \left[\frac{\Delta P}{n} \right]^n \quad (1)$$

with $n = 3$ (Glen's law) and $A \sim 2 \times 10^{-24} \text{ s}^{-1} \text{ Pa}^{-3}$ for ice at the melting point (Cuffey and Patterson, 2010). The maximum value of ΔP is $(D/10 \text{ km}) \times 10^5 \text{ Pa}$ if the ocean is not overpressured. Melt-back by turbulent dissipation can balance inflow and lead to a steady-state conduit aperture, but only if the water flows swiftly (Röthlisberger, 1972; Weertman, 1972; Kite and Rubin, 2016). At steady state, the power consumed in meltback (per unit length pipe) is $2\pi R(\partial R/\partial t)\rho_i L$ (Cuffey and Patterson, 2010), where ρ_i is the density of ice and L is the latent heat of melting. These models assume that water is at the local pressure-melting temperature of ice, and that frictional heat is absorbed locally and instantaneously (Cuffey and Patterson, 2010). Currents driven by flushing of the fractures in response to tidal flexing, given by $2\pi(D)/(1.37 \text{ days})$, where 1.37 days is the orbital period of Enceladus, are roughly 1 m s^{-1} for $D = 20 \text{ km}$, which is sufficient to keep the fractures from closing (Kite and Rubin, 2016).

If the ice shell is decreasing in volume globally over sufficiently fast timescales, the ocean will be underpressured. However, if the ocean is freezing, then it will be overpressured, to the extent that the ice shell can contain the pressure: The maximum ocean overpressure is the tensile strength of ice, 1–3 MPa (Rudolph and Manga, 2009). If the rock core is rigid and impermeable, overpressure of $>10^6 \text{ Pa}$ can be generated (Manga and Wang, 2007). Ocean overpressure/underpressure is important for conduit initiation and conduit stability. For ocean overpressure $> (D/10 \text{ km}) \times 10^5 \text{ Pa}$, conduits will expand by shouldering aside adjacent warm ice, and water can reach the surface even without gas exsolution.

3.2.2. Geometry of the plumbing system. Enceladus' plumbing system could consist of focused flow in slots or channels, distributed porous flow, or something in between. A narrow slot undergoing unidirectional flow is unstable to the formation of discrete pipes (Walder, 1982), but horizontal water transport during tidally pumped flow might suppress this instability (Kite and Rubin, 2016). Pipes may be unstable to elongation perpendicular to the flow direction (Dallaston and Hewitt, 2014). It is difficult for pipes or slots to pinch off at a particular depth because any turbulent dissipation (and thus melt-back) would be focused at the pinch-point. The presence of localized dust jets (Porco et al., 2014), localized gas jets (Hansen et al., 2017; Yeoh et al., 2017), and localized ~ 100 -m-scale hot spots [some of which correlate with apparent jets in visible images; see Goguen et al. (2016) and section 2.2 above] suggest that pipes within

the fissure system may be supplying a significant fraction of the overall heat and mass flux, at least above the water table, where partial blocking by vapor condensation (considered later) may play a role (Nakajima and Ingersoll, 2016).

Closed plumbing systems reaching to just below the surface have also been proposed (Matson et al., 2012). In this model, sensible heat is transferred to the ice and conducted to the surface where it is radiated to space. Bubbles of exsolved CO₂ provide buoyancy on the way up from the ocean, a 2° temperature difference between the warm ocean and the freezing salt water provides the sensible heat, and the gas loss provides the density gain that causes the liquid to sink back to the ocean. The details remain uncertain, but it is clear that a lot of water is involved. The sensible heat associated with a 2° change in temperature is only about 0.3% of the latent heat associated with vaporization. Also, the closed system might be unstable: The pipes might burst and the system could revert to a vapor deposition system.

3.2.3. Sustainability. Models of the Enceladus plumbing system usually assume that it is long-lived. Enceladus' eruptions have been ongoing since at least 2005 (Hedman et al., 2013; Porco et al., 2014), although individual jets do appear to turn on and off (Nimmo et al., 2014) and activity has decreased over the course of the Cassini observations (Ingersoll and Ewald, 2017). The persistence of the E ring, whose grains have a lifetime of decades against sputtering (Jurac et al., 2001), suggests that the current eruption rate is similar to the average over the last ~100 years. The widths of the warm belts bracketing the tiger stripes is ~1 km, as described above. If these belts are kept warm by conductive heating from central fissures, then thermal timescales require the fissures to have been warm for ~10⁴ yr. Finally, complete removal of craters from the SPT probably requires ≫10³ yr of activity. Taken together, the data suggest that the eruptions are sustained but cannot rule out system-wide periods of repose. In either event, the energy transfer from the ocean to the ice shell is so large that it would have a major effect on ice-shell thermal structure.

3.3. Tidal Dissipation and Flexing in the Fracture System

3.3.1. Energy sources. While the distribution of tidal heating within Enceladus is not well established, it is only directly detectable in the south polar region, and is likely to be focused there. Enceladus' internal ocean enhances tidal dissipation by increasing Enceladus' response to gravitational tidal forces. A locally thinner and/or weaker shell may further concentrate heating in the SPT (Souček et al., 2016; Běhounková et al., 2015). Solid ice near its melting point has a viscoelastic response (Maxwell) time comparable to the orbital period of Enceladus, which makes it especially susceptible to tidal heating. This heating will be most effective near the base of the ice shell, where viscosity is lowest.

For some geometries, dissipation of tidally driven flow in the plumbing system could produce power output equal to the observed power output (section 2.4) (see also Kite and

Rubin, 2016). This is analogous to tidal dissipation on Earth, which happens mostly in shallow seas and narrow channels rather than the open ocean or the solid Earth (Egbert and Ray, 2003). The generated power staves off crack freeze-out and helps maintain the ocean against freezing. Kite and Rubin's (2016) model gives a width of 2 m for the water-filled portion of the cracks: In this model a crack with a full width less than 1 m freezes shut. This width is significantly greater than the 0.1-m estimate for cracks in the top tens of meters below the surface derived from the ratio of latent and radiated heat (section 4.2) (see also Ingersoll and Pankine, 2010; Nakajima and Ingersoll, 2016), suggesting that the cracks may narrow toward the surface.

3.3.2. Tidal flexing. The presence of an ocean enhances tidal flexing and generates large tidal stresses on Enceladus' surface. The tiger stripes are approximately aligned with one of the two directions of maximum tidal tensile stresses (Nimmo et al., 2007), suggesting that they may have formed in response to tidal stress. Once formed, these stresses can rework the fractures and control the eruptive activity observed from them.

The strongest direct evidence for tidal control of the eruptive behavior comes from the fact that, as predicted by tidal flexing models (Hurford et al., 2007), the overall plume is brighter at apoapse than at periapse, as seen both by VIMS (Hedman et al., 2013) and ISS (Nimmo et al., 2014; Ingersoll and Ewald, 2017) (Fig. 5). This response is presumably because the opening and closing of cracks modulates the solid mass flux. Plume activity does not cease

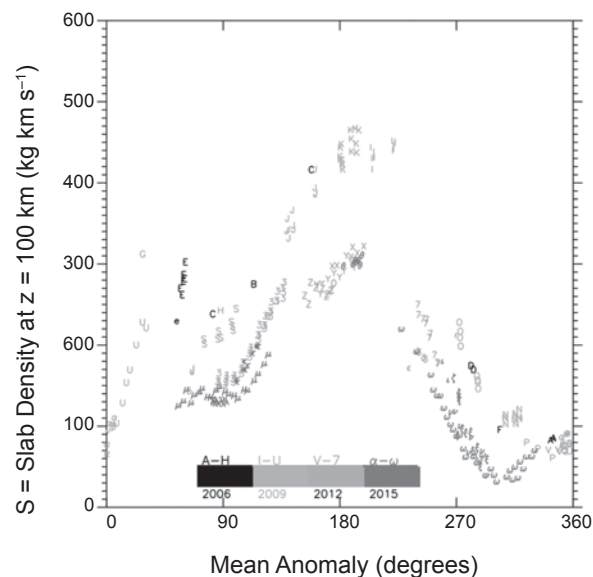


Fig. 5. See Plate 20 for color version. Orbital and long-term variability of the Enceladus dust plume brightness at visible wavelengths, from Ingersoll and Ewald (2017). Different symbols identify different datasets. Mean anomaly describes the orbital position of Enceladus relative to periapse, while the Y axis is a measure of integrated plume brightness at 100 km altitude.

even at periapse, which must indicate either that the cracks do not close entirely (thus placing a lower bound on crack width, if it is uniform), or — less likely — that part of the (solid) plume material emanates from between the tiger stripes. *Nimmo et al.* (2014) conclude that the velocity of the solid material does not appear to change significantly over the orbital period, while *Hedman et al.* (2013) and *Ingersoll and Ewald* (2017) infer a reduction of launch speed around periapse. In contrast, UVIS observations of erupted gas, while sparser, suggest only very small variations in flux with orbital position, but also suggest that the gas velocities may be higher at apoapse (*Hansen et al.*, 2017). Thus, the details of tidal control on eruptive behavior are not yet clear. A further intriguing observation is that the diurnal peak in the eruptive plume lags the predicted peak response of an elastic shell, which is just before apocenter (*Hurford et al.*, 2007, 2012) by several hours (*Nimmo et al.*, 2014; *Ingersoll and Ewald*, 2017). This could be because the shell is responding in a viscoelastic fashion (*Běhounková et al.*, 2015), or perhaps because of the response of water-filled cracks (*Kite and Rubin*, 2016).

On a decadal timescale, the plume appears to be growing fainter (*Hedman et al.*, 2013; *Ingersoll and Ewald*, 2017) (Fig. 5), which suggests a decreasing solid mass flux. This could be due to some change in the plumbing, but may also be an effect of subtle 11-year periodic variations in orbital parameters (*Horanyi et al.*, 1992; *Vienne and Duriez*, 1992) or (less likely) seasonal insolation-driven changes in the near-surface temperature. To date, no such long-period variation is evident in the vapor flux estimates (*Hansen et al.*, 2017).

3.3.3. Energy balance within the fractures. Given the apparently low shell thickness at the SPT (*Čadek et al.*, 2016), the possible broad regional heat flow between the tiger stripes, hinted at in the CIRS data (section 2.4), is probably transferred to the surface via conduction. However, the highly localized heat fluxes along the tiger stripes indicate that there must be additional processes operating. An isothermal crack at temperatures above ~ 200 K will transfer heat to the surroundings, generating a local thermal anomaly similar to that observed (*Abramov and Spencer*, 2009). Transfer of heat from the water-filled or vapor-filled fracture to the surroundings occurs primarily by deposition of latent heat (*Ingersoll and Pankine*, 2010). This is because, as heat flows away by conduction from the ice fracture walls to balance radiation at the surface, any reduction in wall temperature will immediately result in condensation or freezing of water onto the walls to maintain isothermality. In the absence of competing processes, such as local dissipation and melt-back, this deposition inexorably narrows the fractures. Below the water surface, the heat comes from the latent heat of fusion as water freezes onto the fracture walls. *Ingersoll and Nakajima* (2016) parameterize the heat conduction using the formula $F = 4k_i\Delta T/(\pi z)$, where F is the heat flux into the wall, k_i is the thermal conductivity of ice, ΔT is the temperature difference between the warm wall and the cold surface, and z is the depth. The formula is valid for an isothermal crack and an isothermal surface.

The upward speed of the water column is assumed to match that required to balance condensation of vapor near the surface, determined by the total radiated power (assumed in this paper to be ~ 4.7 GW) divided by the 500-km length of the tiger stripes and by the latent heat of vaporization. The result is that the water loses slightly more than half its mass in going from the ocean to the evaporating surface. It also means the build-up of ice is closing the crack at a rate of 5.4 cm yr $^{-1}$, about 10% of the rate above the water surface (section 4.2). The flushing that accompanies the opening and closing of the cracks will counteract this freezing (*Kite and Rubin*, 2016).

4. PHYSICS OF THE PLUME VENTS AT AND ABOVE THE PRESUMED LIQUID INTERFACE

4.1. The Water/Vapor Interface

Much of the important physics in the plume plumbing occurs at the water surface within the fractures. At least some of the plume particles are probably created here, giving us direct samples from this location, and the fact that this interface appears to resist freezing over, at least on short timescales, provides key constraints on plume physics.

Evaporative cooling will tend to rapidly freeze the water surface, which would shut down the eruptions. Ice forms when liquid water at 0°C evaporates, producing 7.5 g of ice for every 1 g of vapor, based on the heats of vaporization and fusion. Fresh water has a density maximum at 4.3°C , so the freezing water accumulates at the surface — it is not replaced by warmer water from below (water with salinity greater than 24.7 g kg $^{-1}$ does not have this problem — the densest water is at the freezing point). Several solutions to the evaporative cooling problem have been proposed. Each involves exchange with a deeper thermal bath, such as the ocean:

1. If the surface area that is evaporating is much larger than the vent cross-sectional area, then the evaporative power (W m^{-2} of evaporating area) is modest due to the vapor pressure above the water surface, and can be balanced by convective exchange with a deeper reservoir (*Postberg et al.*, 2009). This requires large vapor chambers above the liquid that narrow to the vent channels. However, *Ingersoll and Nakajima* (2016) and *Nakajima and Ingersoll* (2016) point out that even if the walls are parallel, friction with the walls of a long, narrow channel produces a backpressure that is almost as large as the saturation vapor pressure of the liquid. A stable equilibrium develops — too much flow causes the backpressure to increase, and that reduces the evaporation rate. Too little flow and the backpressure will decrease, causing faster evaporation.

2. Evaporative cooling at the top of a constant-width slot can be balanced by convective overturn, if the water has salinity >16.2 g kg $^{-1}$ and is stirred near the water table by exsolving bubbles (*Ingersoll and Nakajima*, 2016). In this model, evaporation of salty water leaves colder, saltier, and thus denser water behind, which sinks and brings warmer, fresher water to the surface. Since 20 g kg $^{-1}$ is the upper limit

of the measured range (Postberg et al., 2009), Ingersoll and Nakajima (2016) concluded that narrow conduits filled with salty liquid could support the plumes observed at the surface.

3. Dissipation of kinetic energy due to tidal pumping will delay and may prevent icing over (Kite and Rubin, 2016).

4. Siphoning driven by the exsolution of exsolved gases could bring warm gas-charged fluid from the ocean to the water table, with cold degassed water sinking back to the ocean (Matson et al., 2012).

Approaches 1–3 above share the requirement that conduit width below the water table is ≥ 0.1 m; the results of Nakajima and Ingersoll (2016) suggest that the slot width above the water must be less than that below. Approaches 2–4 share the feature that water circulates between the ice shell and the ocean. If water that has changed its temperature and composition during its passage through the ice shell returns to the ocean, this will affect ocean-top temperature and composition (Melosh et al., 2004).

As discussed in section 3.1, the characteristics of the plumes' particles and gases are clues to the physical and chemical processes at the ocean-gas interface. Early estimates of a high solids-to-vapor ratio in the plume led to comparisons to a Yellowstone geyser, where a bubbly liquid erupts into a low-pressure environment (Porco et al., 2006). The low solubility in water of methane and other alkanes led to theories of explosive dissociation of clathrate hydrates containing gases physically trapped in the lattice (Kieffer et al., 2006; Gioia et al., 2007). The geyser model suffers because the particles don't go high enough (Brilliantov et al., 2008), and is also ruled out by the lack of the sodium vapor that would be expected from explosive evaporation of water containing dissolved sodium salts (Schneider et al., 2009; Postberg et al., 2011). The clathrate model suffers because water vapor is a minor component of clathrate decomposition — a substantial part of the water vapor in the plumes would come from sublimation of ice grains in a flow driven by the volatile-entrapped gases, including CO_2 , N_2 , CO , and CH_4 (Postberg et al., 2011). Postberg et al. (2009, 2011) argue that the liquid water reservoir is wide and close to the surface, such that droplets from the ocean spray can freeze and be ejected as plume particles. Additional models of the plume generation process are still being actively developed (e.g., Matson et al., 2012; Kite and Rubin, 2016).

Micrometer-sized particles can be launched from the ocean and entrained into the plume gas by controlled boiling involving bubbles breaking at the surface, which generates spray (Ingersoll and Nakajima, 2016; Porco et al., 2017). There are two mechanisms for launching droplets. Film droplets form when the thin upper surface of a bubble, protruding into the air, shatters into hundreds of particles with radii ranging between ~ 0.01 μm and 1 – 2 μm . Jet droplets form when the bubble cavity collapses; several droplets are formed in a vertical column with radii in the ~ 1 – 50 - μm range (de Leeuw et al., 2011; Veron, 2015). These sizes overlap with those of particles in the Enceladus plumes (Hedman et al., 2009; Ingersoll and Ewald, 2011; Postberg et al., 2011).

There is abundant evidence for plume jets from multiple sources. The CDA data imply three compositional types (Postberg et al., 2011). Type I grains are almost pure water ice. Type II grains contain organic compounds and/or silicates. Type III grains are rich in sodium and potassium salts, are more massive, and are concentrated close to the surface, suggesting they are launched at speeds less than the escape velocity. UVIS and INMS data imply both distributed sources along the tiger stripes and narrow jets with Mach numbers >5 (Yeoh et al., 2015, 2017). These patterns may imply that sources extending to the ocean have large particles rich in salt and leave the vent at slower speeds. Or it is possible that all the sources are the same and the large particles intrinsically have slower speeds? Schmidt et al. (2008) and Postberg et al. (2011) pursue the latter assumption. In their model, the particles are constantly having their speeds reset to zero by collisions with the walls of the conduits, which are assumed to have variable cross-section. The collision rate is the same for all particles, but the time to reaccelerate back to the speed of the gas is greater for the larger particles. The authors get a good fit to the particle size distribution and the preponderance of larger, slower, particles close to the surface with a distance between collisions of about 0.1 m. This is comparable to the widths of the conduits, according to some models (Ingersoll and Pankine, 2010; Nakajima and Ingersoll, 2016).

4.2. Escape to the Surface

There are two pathways by which heat generated inside Enceladus is lost to space (Ingersoll and Pankine, 2010). One is infrared radiation emitted at the surface, discussed above. The other is the latent heat of vaporization associated with the ~ 220 kg s^{-1} of water vapor escaping from the vents (Hansen et al., 2011, 2017). Assuming a heat of vaporization of 2.5×10^6 J kg^{-1} , the latent heat power is 0.55 GW, about 13% of the tiger stripe infrared power of ~ 4.2 GW. The ratio of these two pathways provides a useful constraint on the width of the conduit. Assuming that the heat radiated to space comes from the freezing and condensation on the walls, the infrared power will not change with crack width but the latent heat associated with the escaping vapor will. Using a fluid dynamical model of vapor-filled cracks, Ingersoll and Pankine (2010) and Nakajima and Ingersoll (2016) derived a crack width of ~ 0.1 m extending over the 500-km cumulative length of the tiger stripes in order to match the observed ratio. A larger width would give a larger ratio of latent heat to infrared emission, and that was not observed. However, very close to the surface, the vents appear to flare, probably due to sublimation of the water ice: Goguen et al. (2013) estimate a width of 9 m for the fracture at a hot spot on Baghdad Sulcus.

The vapor-filled vent will self-seal rapidly due to deposition of latent heat as discussed above (Ingersoll and Pankine, 2010). Figure 3 shows that the hot component of the model fit to the Cassini CIRS data, which will preferentially be radiated close to the vent and thus from shallow depths, has a typical temperature of about 140 K and emission width

of about 200 m (i.e., 100 m either side of the fractures, if symmetrical). If this radiated power were supplied by deposition of latent heat in the uppermost 100 m of the fracture, the deposition rate would be 0.3 m per year. If this were the only process, a crack 0.1 m wide would close shut in a few months. Condensation near the top is likely because thermal conduction through the ice to the surface is greatest there, and the walls are likely to be colder down to a depth that is comparable to the radiating strip. Ice flow at depth may contribute to keeping the near-surface fractures open, as discussed in section 5.1. Mechanical erosion due to differential tidal motion of the fracture walls may also play a role.

5. BROADER IMPLICATIONS

5.1. Tectonic Setting

We do not currently know how processes at the tiger stripes relate to the larger-scale tectonics of the south polar region (see the chapter in this volume by Patterson et al.). The overall energy budget of the SPT is strongly influenced by advection: ascent of warm water through cracks and shallow deposition of ice releasing latent heat. But there is also likely to be a significant background contribution from heat conducted across the ice shell. Such a regime would be intermediate between the tectonics of Earth (energy loss dominated by conduction) and the tectonics of Io (energy loss dominated by magmatic advection).

Feedbacks between cryovolcanism and tectonics are likely. For example, ice inflow into the base of the conduits, if sustained for $>10^6$ yr, would cause regional subsidence (Kite and Rubin, 2016). This subsidence may indirectly create accommodation space near the fractures, perhaps keeping them open in the face of ice condensation (Fig. 6). This model would predict negligible heat flow between the tiger stripes, due to the subsidence.

Intermittent tectonic resurfacing (O'Neill and Nimmo, 2010) could both cause and be caused by cryovolcanic regime shifts. If the tiger stripe thermal emission is carried by latent heat deposited by condensation on the walls of the tiger stripe (Ingersoll and Pankine, 2010; Porco et al., 2014), the flow of mass from the water source to the topmost kilometer of the ice shell, $\sim 2 \times 10^3 \text{ kg s}^{-1}$, is (if not transmitted downward by subsidence) equivalent to an expansive strain distributed across the whole tiger stripe terrain of $\sim 10^{-13} \text{ s}^{-1}$. Such a strain would double the width of the SPT in ~ 3 m.y. If this situation is maintained long term, cryovolcanic mass and energy fluxes are comparable to tectonic mass and energy fluxes, so that cryovolcanism and tectonics are strongly coupled. Three-dimensional models are now being applied to the ductile (Běhouňková et al., 2015) and brittle (Souček et al., 2016) behaviors of the solid ice shell, but these three-dimensional models have not yet been combined with each other, nor with feedbacks on the liquid-water plumbing system.

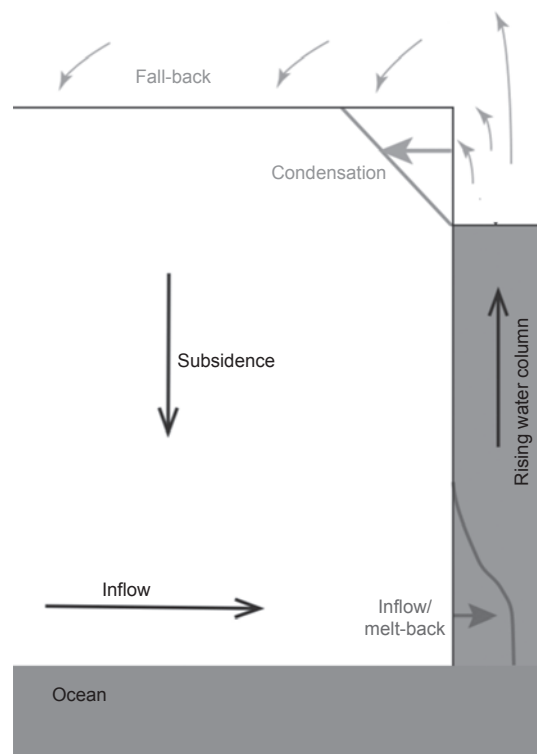


Fig. 6. Schematic of possible flow in the ice shell surrounding the tiger stripes, adapted from Kite and Rubin (2016). In this model, melt-back due to turbulent dissipation in the water-filled portion of the tiger stripes (right) causes subsidence of the ice shell, which opens the vapor-filled portion of the fractures near the surface, perhaps preventing them from self-sealing due to ice condensation.

5.2. Astrobiology

For astrobiology, the message from plumbing-system modeling is that the salt-rich jets of Enceladus represent a fresh sample of the ocean. There is no reason to expect that water sits in cryomagma chambers inside the ice shell for long timescales that might lead to the breakdown of biomarkers. Progress on the volcano-tectonic connection will also constrain the rate at which oxidants produced at Enceladus' surface by radiation-driven chemistry are recycled into Enceladus' ocean: potentially a source of energy for life at Europa (Vance et al., 2016) and perhaps at Enceladus too (Parkinson et al., 2008). Bubbles near the water-vapor interface may concentrate biological material, if any, and carry it into the plume (Porco et al., 2017).

6. SUMMARY AND OPEN QUESTIONS

We have learned a lot about the plume fractures and vents in the dozen years since the discovery of activity. Fractures appear to cut through the entire thickness of the ice shell, and are likely mostly filled with liquid water, connected directly to the ocean. Water circulation at speeds of about 1 m s^{-1} , driven by tidal flexing in fractures roughly

1 m wide, may generate enough dissipation to match much of the observed power radiated by the tiger stripes, and the resulting melt-back may combat fracture narrowing by viscous creep and the expected freezing of water onto the fracture walls required to balance conductive heat loss. At the water surface, expected from buoyancy arguments to be situated ~10% of the way down to the ocean, observed plume particles may be generated by bursting of bubbles. Freezing of the water surface by evaporative cooling may be avoided by water vapor pressure buildup above the water surface, due to a combination of narrowing of the fractures toward the surface and viscous throttling of the escaping vapor in the fractures, and also by salinity-driven overturn or dissipative heating of the water. The upper, vapor-filled, part of the fractures may have typical widths of 0.1 m. However, rapid condensation of water vapor onto the fracture walls is expected to narrow the fractures by $\sim 0.3 \text{ m yr}^{-1}$, raising unanswered questions about their long-term stability. This condensation transfers several Gigawatts of latent heat to the fracture walls, where it is conducted to the surface and radiated to space, while a smaller fraction escapes directly as latent heat. Near-surface temperatures approach 200 K, probably limited by sublimation cooling.

However, many outstanding questions remain about the plume origins and plumbing. One is the spatial distribution of heat, solid, and vapor sources. For instance, are the solids lofted mainly in jets or in curtains? Are there vapor sources that do not produce significant solids? How continuous is the emission of heat, solids, and vapor along the tiger stripes? And in particular, what is the magnitude of the likely background-distributed heat source between the tiger stripes?

Space-time variability of the plume and its jets is not fully understood. While individual jets do appear to turn on and off (Porco et al., 2014), unlike the plume as a whole, they do not do so in a manner explicable by simple tidal models; instead, choking of conduits by ice deposition in the near-surface, and subsequent opening of new channels, may be the culprit. Are vapor and solids modulated by tides in the same way? It is not clear why the plume persists at periapse when tidal forces should close the fractures, or why there is a time lag in the orbital response. Also, the origin of the secular decrease in plume brightness seen during the Cassini mission (Ingersoll and Ewald, 2017) remains a mystery.

We do not understand the width and shape of the cracks. To keep them from freezing, widths of 1 m are best for the water-filled parts of the channels (Ingersoll and Nakajima, 2016; Kite and Rubin, 2016). Widths of 0.1 m are best for the vapor-filled parts of the channels to match the latent heat to radiation ratio (Nakajima and Ingersoll, 2016) and to match the particle sorting with altitude (Schmidt et al., 2008; Postberg et al., 2011). But these are model-dependent results with limited observational confirmation to date.

While continued analysis of the rich legacy of Cassini observations may answer many of these questions, some must await the next mission to Enceladus, which we hope will occur within the next few decades.

REFERENCES

- Abramov O. and Spencer J. R. (2009) Endogenic heat from Enceladus' south polar fractures: New observations and models of conductive surface heating. *Icarus*, 199, 189–196.
- Běhouňková M., Tobie G., Čadek O., Choblet G., Porco C., and Nimmo F. (2015) Timing of water plume eruptions on Enceladus explained by interior viscosity structure. *Nature Geosci.*, 8, 601–604.
- Brilliantov N. V., Schmidt J., and Spahn F. (2008) Geysers of Enceladus: Quantitative analysis of qualitative models. *Planet. Space Sci.*, 56, 1596–1606.
- Čadek O. and 10 colleagues (2016) Enceladus's internal ocean and ice shell constrained from Cassini gravity, shape, and libration data. *Geophys. Res. Lett.*, 43, 5653–5660.
- Cooper J. F., Cooper P. D., Sittler E. C., Sturmer S. J., and Rymer A. M. (2009) Old Faithful model for radiolytic gas-driven cryovolcanism at Enceladus. *Planet. Space Sci.*, 57, 1607–1620.
- Crawford G. D. and Stevenson D. J. (1988) Gas-driven water volcanism in the resurfacing of Europa. *Icarus*, 73, 66–79.
- Cuffey K. and Patterson W. (2010) *The Physics of Glaciers, 4th edition*. Elsevier (Academic), New York.
- Dallaston M. C. and Hewitt I. J. (2014) Free-boundary models of a meltwater conduit. *Phys. Fluids*, 26, article ID 083101.
- de Leeuw G., Andreas E. L., Anguelova M. D., Fairall C. W., Lewis E. R., O'Dowd C., Schulz M., and Schwartz S. E. (2011) Production flux of sea spray aerosol. *Rev. Geophys.*, 49, RG2001, DOI: 10.1029/2010RG000349.
- Dougherty M. K., Khurana K. K., Neubaur F. M., Russell C. T., Saur J., Leisner J. S., and Burton M. E. (2006) Identification of a dynamic atmosphere at Enceladus with the Cassini magnetometer. *Science*, 311, 1406–1409.
- Egbert G. D. and Ray R. D. (2003) Semi-diurnal and diurnal tidal dissipation from TOPEX/Poseidon altimetry. *Geophys. Res. Lett.*, 30, 1907.
- Gao P., Koppa P., Zhang X., and Ingersoll A. P. (2016) Aggregate particles in the plumes of Enceladus. *Icarus*, 264, 227–238.
- Gioia G., Chakrobarty P., Marshak S., and Kieffer S. W. (2007) Unified model of tectonics and heat transport in a frigid Enceladus. *Proc. Natl. Acad. Sci.*, 104, 13578–13581.
- Glein C. R., Zolotov M. Y., and Shock E. L. (2008) The oxidation state of hydrothermal systems on early Enceladus. *Icarus*, 197, 157–163.
- Glein C. R., Baross J. A., and Waite J. H. (2015) The pH of Enceladus' ocean. *Geochim. Cosmochim. Acta*, 162, 202–219.
- Goguen J. D. and 12 colleagues (2013) The temperature and width of an active fissure on Enceladus measured with Cassini VIMS during the 14 April 2012 south pole flyover. *Icarus*, 226, 1128–1137.
- Goguen J. D., Buratti B. J., and the Cassini VIMS Team (2016) Cassini VIMS spectra of the thermal emission from hot spots along Enceladus south pole fissures. *AAS/Division for Planetary Sciences Meeting Abstracts*, 48, 214.10.
- Gorini N., Howett C., Spencer J., Albright S., Jennings D., Hurford T., Romani P., Segura M., and Verbiscer A. (2015) Resolving Enceladus thermal emission at the 10s of meters scale along Baghdad Sulcus using Cassini CIRS. *AAS/Division for Planetary Sciences Meeting Abstracts*, 47, 410.01.
- Hansen C. J. and 10 colleagues (2011) The composition and structure of the Enceladus plume. *Geophys. Res. Lett.*, 38, L11202.
- Hansen C. J., Esposito L. W., Aye K.-M., Colwell J. E., Hendrix A. R., Portyankina G., and Shemansky D. (2017) Investigation of diurnal variability of water vapor in Enceladus' plume by the Cassini ultraviolet imaging spectrograph. *Geophys. Res. Lett.*, 44, 672–677.
- Hedman M. M., Nicholson P. D., Showalter M. R., Brown R. H., Buratti B. J., and Clark R. N. (2009) Spectral observations of the Enceladus plume with Cassini-VIMS. *Astrophys. J.*, 693, 1749–1762.
- Hedman M. M., Gosmeyer C. M., Nicholson P. D., Sotin C., Brown R. H., Clark R. N., Baines K. H., Buratti B. J., and Showalter M. R. (2013) An observed correlation between plume activity and tidal stresses on Enceladus. *Nature*, 500, 182–184.
- Helfenstein P. and Porco C. C. (2015) Enceladus' geysers: Relation to geological features. *Astron. J.*, 150, 96.
- Horanyi M., Burns J. A., and Hamilton D. P. (1992) The dynamics of Saturn's E ring particles. *Icarus*, 97, 248–259.

- Howett C. J. A., Spencer J. R., Pearl J., and Segura M. (2011) High heat flow from Enceladus' south polar region measured using 10–600 cm⁻¹ Cassini/CIRS data. *J. Geophys. Res.–Planets*, 116, E03003.
- Hsu H.-W. and 14 colleagues (2015) Ongoing hydrothermal activities within Enceladus. *Nature*, 519, 207–210.
- Hurford T. A., Helfenstein P., Hoppa G. V., Greenberg R., and Bills B. G. (2007) Eruptions arising from tidally controlled periodic openings of rifts on Enceladus. *Nature*, 447, 292–294.
- Hurford T. A., Helfenstein P., and Spitalo J. N. (2012) Tidal control of jet eruptions on Enceladus as observed by Cassini ISS between 2005 and 2007. *Icarus*, 220, 896–903.
- Iess L. and 10 colleagues (2014) The gravity field and interior structure of Enceladus. *Science*, 344, 78–80.
- Ingersoll A. P. and Ewald S. P. (2011) Total particulate mass in Enceladus plumes and mass of Saturn's E ring inferred from Cassini ISS images. *Icarus*, 216, 492–506.
- Ingersoll A. P. and Ewald S. P. (2017) Decadal timescale variability of the Enceladus plumes inferred from Cassini images. *Icarus*, 282, 260–275.
- Ingersoll A. P. and Nakajima M. (2016) Controlled boiling on Enceladus. 2. Model of the liquid-filled cracks. *Icarus*, 272, 319–326.
- Ingersoll A. P. and Pankine A. A. (2010) Subsurface heat transfer on Enceladus: Conditions under which melting occurs. *Icarus*, 206, 594–607.
- Jurac S., Johnson R. E., and Richardson J. D. (2001) Saturn's E ring and production of the neutral torus. *Icarus*, 149, 384–396.
- Kieffer S. W., Lu X., Bethke C. M., Spencer J. R., Marshak S., and Navrotsky A. (2006) A clathrate reservoir hypothesis for Enceladus' south polar plume. *Science*, 314, 1764.
- Kieffer S. W., Lu X., McFarquhar G., and Wohletz K. H. (2009) A redetermination of the ice/vapor ratio of Enceladus' plumes: Implications for sublimation and the lack of a liquid water reservoir. *Icarus*, 203, 238–241.
- Kite E. S. and Rubin A. M. (2016) Sustained eruptions on Enceladus explained by turbulent dissipation in tiger stripes. *Proc. Natl. Acad. Sci.*, 113, 3972–3975.
- Le Gall A. and 17 colleagues (2017) Thermally anomalous features in the subsurface of Enceladus's south polar terrain. *Nature Astron.*, 1, 0063.
- Loeffler M. J., Raut U., and Baragiola R. A. (2006) Enceladus: A source of nitrogen and an explanation for the water vapor plume observed by Cassini. *Astrophys. J.*, 649, L133–L136.
- Manga M. and Wang C.-Y. (2007) Pressurized oceans and the eruption of liquid water on Europa and Enceladus. *Geophys. Res. Lett.*, 34, L07202.
- Matson D. L., Castillo J. C., Lunine J., and Johnson T. V. (2007) Enceladus' plume: Compositional evidence for a hot interior. *Icarus*, 187, 569–573.
- Matson D. L., Castillo-Rogez J. C., Davies A. G., and Johnson T. V. (2012) Enceladus: A hypothesis for bringing both heat and chemicals to the surface. *Icarus*, 221, 53–62.
- Melosh H. J., Ekhöf A. G., Showman A. P., and Lorenz R. D. (2004) The temperature of Europa's subsurface water ocean. *Icarus*, 168, 498–502.
- Nakajima M. and Ingersoll A. P. (2016) Controlled boiling on Enceladus. 1. Model of the vapor-driven jets. *Icarus*, 272, 309–318.
- Nimmo F., Spencer J. R., Pappalardo R. T., and Mullen M. E. (2007) Shear heating as the origin of the plumes and heat flux on Enceladus. *Nature*, 447, 289–291.
- Nimmo F., Porco C. P., and Mitchell C. (2014) Tidally modulated eruptions on Enceladus: Cassini ISS observations and models. *Astron. J.*, 148, DOI: 10.1088/0004-6256/148/3/46.
- Nye J. F. (1953) The flow law of ice from measurements in glacier tunnels, laboratory experiments and the Jungfraufirn borehole experiment. *Proc. R. Soc. London*, 1139, 477–489.
- O'Neill C. and Nimmo F. (2010) The role of episodic overturn in generating the surface geology and heat flow on Enceladus. *Nature Geosci.*, 3, 88–91.
- Parkinson C. D., Liang M.-C., Yung Y. L., and Kirschvink J. L. (2008) Habitability of Enceladus: Planetary conditions for life. *Origins Life Evol. Biosph.*, 38, 355–369.
- Porco C. C., Helfenstein P., Thomas P. C., Ingersoll A. P., Wisdom J., et al. (2006) Cassini observes the active south pole of Enceladus. *Science*, 311, 1393–1401.
- Porco C., Di Nino D., and Nimmo F. (2014) How the geysers, tidal stresses, and thermal emission across the south polar terrain of Enceladus are related. *Astron. J.*, 148, 45.
- Porco C. C., Dones L., and Mitchell C. (2017) Could it be snowing microbes on Enceladus? Assessing conditions in its plume and implications for future missions. *Astrobiology*, 17(9), DOI: 10.1089/ast.2017.1665.
- Postberg F., Kempf S., Schmidt J., Brilliantov N., Beinsen A., Abel B., Buck U., and Srama R. (2009) Sodium salts in E-ring ice grains from an ocean below the surface of Enceladus. *Nature*, 459, 1098–1101.
- Postberg F., Schmidt J., Hillier J., Kempf S., and Srama R. (2011) A salt-water reservoir as the source of a compositionally stratified plume on Enceladus. *Nature*, 474, 620–622.
- Röthlisberger H. (1972) Water pressure in intra- and subglacial channels. *J. Glaciol.*, 11, 177–203.
- Rubin A. M. (1995) Propagation of magma-filled cracks. *Annu. Rev. Earth Planet. Sci.*, 23, 287–336.
- Rudolph M. L. and Manga M. (2009) Fracture penetration in planetary ice shells. *Icarus*, 199, 536–541.
- Schmidt J., Brilliantov N., Spahn F., and Kempf S. (2008) Slow dust in Enceladus' plume from condensation and wall collisions in tiger stripe fractures. *Nature*, 451, 685–688.
- Schneider N. M., Burger M. H., Schaller E. L., Brown M. E., Johnson R. E., et al. (2009) No sodium in the vapour plumes of Enceladus. *Nature*, 459, 1102–1104.
- Schulson E. M. (2001) Brittle failure of ice. *Eng. Fracture Mech.*, 68, 1839–1887.
- Sekine Y. and 11 colleagues (2015) High-temperature water-rock interactions and hydrothermal environments in the chondrite-like core of Enceladus. *Nature Commun.*, 6, 8604.
- Souček O., Hron J., Běhounková M., and Čadež O. (2016) Effect of the tiger stripes on the deformation of Saturn's moon Enceladus. *Geophys. Res. Lett.*, 43, 7417–7423.
- Spencer J. R. and Nimmo F. (2013) Enceladus: An active ice world in the Saturn system. *Annu. Rev. Earth Planet. Sci.* 41, 693–717.
- Spencer J. R., Pearl J. C., Segura M., Flasar F. M., Mamoutkine A., Romani P., Buratti B. J., Hendrix A. R., Spilker L. J., and Lopes R. M. C. (2006) Cassini encounters Enceladus: Background and the discovery of a south polar hot spot. *Science*, 311, 1401–1405.
- Spencer J. R., Howett C. J. A., Verbiscer A. J., Hurford T. A., Segura M. E., and Pearl J. C. (2011) Observations of thermal emission from the south pole of Enceladus in August 2010. *EPSC-DPS Joint Meeting 2011*, 1630.
- Spencer J. R., Howett C. J. A., Verbiscer A., Hurford T. A., Segura M., and Spencer D. C. (2013) Enceladus heat flow from high spatial resolution thermal emission observations. *EPSC 2013 Abstracts*, 8–13 September, London, UK.
- Spitalo J. N. and Porco C. C. (2007) Association of the jets of Enceladus with the warmest regions on its south-polar fractures. *Nature*, 449, 695–697.
- Spitalo J. N., Hurford T. A., Rhoden A. R., Berkson E. E., and Platts S. S. (2015) Curtain eruptions from Enceladus' south-polar terrain. *Nature*, 521, 57–60.
- Vance S. D., Hand K. P., and Pappalardo R. T. (2016) Geophysical controls of chemical disequilibria in Europa. *Geophys. Res. Lett.*, 43, 4871–4879.
- Veeder G. J., Matson D. L., Johnson T. V., Blaney D. L., and Goguen J. D. (1994) Io's heat flow from infrared radiometry: 1983–1993. *J. Geophys. Res.*, 99, 17095–17162.
- Veron F. (2015) Ocean spray. *Annu. Rev. Fluid Mech.*, 47, 507–538.
- Vienne A. and Duriez L. (1992) A general theory of motion for the eight major satellites of Saturn III. Long-period perturbations. *Astron. Astrophys.*, 257, 331–352.
- Waite J. H. Jr. and 15 colleagues (2009) Liquid water on Enceladus from observations of ammonia and ⁴⁰Ar in the plume. *Nature*, 460, 487–490.
- Waite J. H. and 12 colleagues (2017) Cassini finds molecular hydrogen in the Enceladus plume: Evidence for hydrothermal processes. *Science*, 356, 155–159.
- Walder J. (1982) Stability of sheet flow of water beneath temperate glaciers and implications for glacier surging. *J. Glaciol.*, 28, 273–293.
- Weertman J. (1972) General theory of water flow at the base of a glacier or ice sheet. *Rev. Geophys. Space Phys.*, 10, 287–333.
- Yeoh S. K., Chapman T. A., Goldstein D. B., Varghese P. L., and Trafton L. M. (2015) On understanding the physics of the Enceladus south polar plume via numerical simulation. *Icarus*, 253, 205–222.
- Yeoh S. K., Li Z., Goldstein D. B., Varghese P. L., Levin D. A., and Trafton L. M. (2017) Constraining the Enceladus plume using numerical simulation and Cassini data. *Icarus*, 281, 357–378.

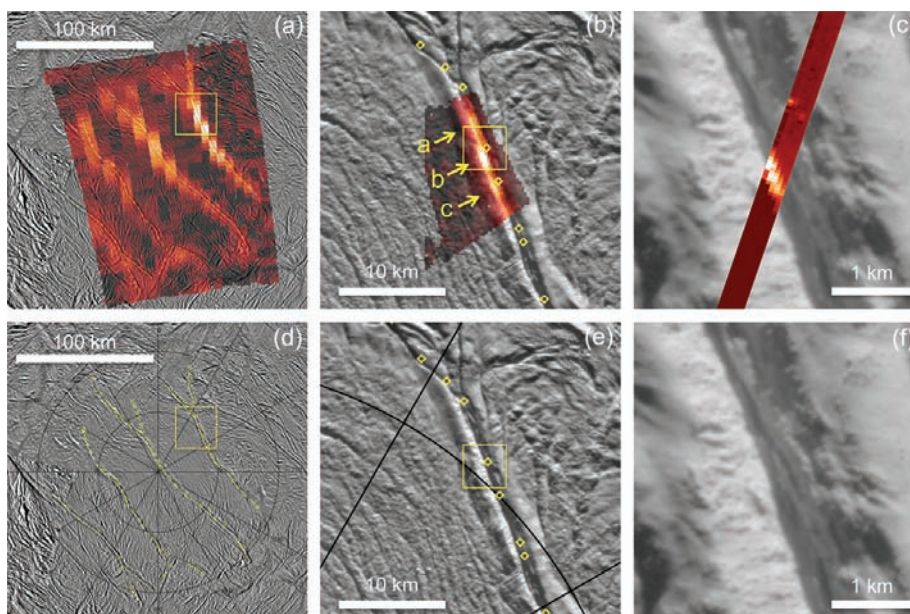


Plate 19. The appearance of the tiger stripes in the visible (Cassini ISS) and thermal infrared [Cassini CIRS, 7–16 μm , (a)–(c)] at a variety of scales. (a) The entire tiger stripe system with the exception of part of Alexandria Sulcus (left), which is known from other observations to be relatively faint. CIRS 9–16- μm data from March 2008. Dashed lines mark the location of the active tiger stripes. The square shows the location of (b). (b) Closeup of the most active part of Damascus Sulcus (a combination of 9–16- μm and 7–9- μm images), mapped by CIRS in August 2010. Diamonds show the location of ISS plume jets reported by *Helfenstein and Porco (2015)*. Arrows mark the locations of three discrete hot spots, a, b, and c (also shown in Fig. 2a), two of which correspond well to plume jet locations. The square shows the location of (c). (c) The highest-resolution CIRS image of Damascus Sulcus emission, taken by direct sampling of the CIRS 7–9- μm interferograms from October 2015, showing dominant emission from a single fissure <100 m wide, and isolated hot spots elsewhere within the central trough (*Gorius et al., 2015*). Placement relative to the terrain is approximate. (d)–(f) The same images without the CIRS data overlay, to show the terrain more clearly.

Accompanies chapter by Spencer et al. (pp. 163–174).

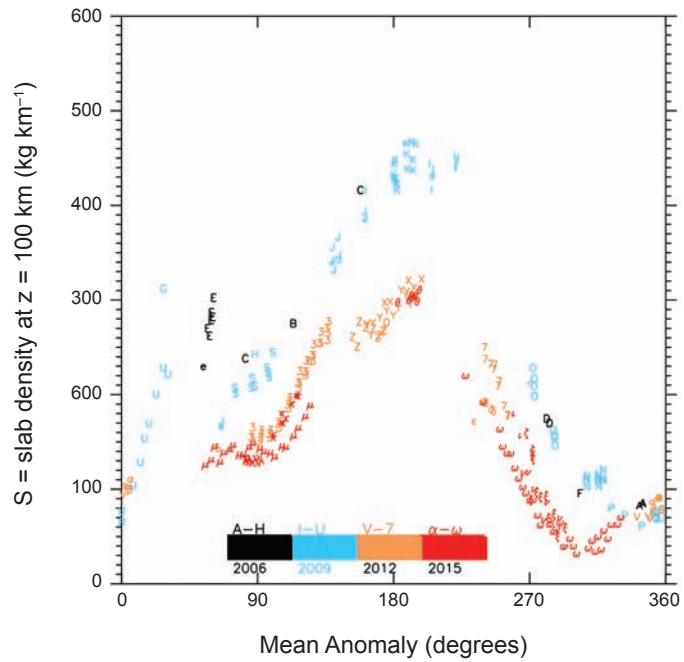


Plate 20. Orbital and long-term variability of the Enceladus dust plume brightness at visible wavelengths, from *Ingersoll and Ewald* (2017). Different symbols identify different datasets. Mean anomaly describes the orbital position of Enceladus relative to periapse, while the Y axis is a measure of integrated plume brightness at 100 km altitude.

Accompanies chapter by Spencer et al. (pp. 163–174).